Photofission of heavy nuclei from 0.2 to 3.8 GeV

C. Cetina, P. Heimberg, B. L. Berman, W. J. Briscoe, G. Feldman, and L. Y. Murphy
Center for Nuclear Studies, Department of Physics, The George Washington University, Washington, D.C. 20052

Hall Crannell, A. Longhi,* and D. I. Sober
Department of Physics, The Catholic University of America, Washington, D.C. 20064

J. C. Sanabria
Department of Physics, Universidad de los Andes, A.A. 4976, Bogota, Colombia

G. Ya. Kezerashvili†
Budker Institute of Nuclear Physics, 630090 Novosibirsk, Russia
(Received 27 December 2001; published 10 April 2002)

Total photofission cross sections for ^{237}Np, ^{233}U, ^{235}U, ^{238}U, ^{232}Th, and ^{nat}Pb have been measured simultaneously, using tagged photons in the energy range $E_\gamma = 0.17-3.84$ GeV in Hall B at Jefferson Lab. The fission fragments were detected using parallel-plate avalanche detectors. Our results show that, of these nuclei, ^{237}Np has the largest photofission cross section per nucleon, and that the photofission cross section for ^{238}U relative to that for ^{237}Np is about 80% over the entire energy range. The relative photofission cross sections per nucleon increase with the fissility parameter Z^2/A, approaching an apparent asymptote at the Z^2/A value for ^{237}Np, and they do not depend strongly on the incident photon energy over this entire energy range. These results, together with a comparison of the ^{237}Np photofission cross section per nucleon with total photoabsorption data, indicate that the photofission probability for ^{237}Np is almost unity. If we make this assumption, we observe a significant shadowing of the interior nucleons starting below 1.5 GeV, so that the photoabsorption cross section decreases by 20% near 4 GeV.

DOI: 10.1103/PhysRevC.65.044622 PACS number(s): 25.85.Jg, 25.20.Dc

I. INTRODUCTION

The absorption of photons by nuclei is often used to study the modifications induced by the nuclear medium on hadron properties and photon-nucleon interactions. For light nuclei, photoabsorption is investigated experimentally either by using single-particle reactions or by measuring the total photoabsorption cross section $\sigma_{\gamma,A}$. For heavy nuclei, fission is an important decay channel and, as E_γ increases, the induced fission probability increases rapidly towards unity, from the region of the giant dipole resonance [1–3]. It has been a common belief [4–6] that for uranium and transuranic isotopes and for incident photon energies above 50 MeV, the total photofission cross section $\sigma_{\gamma,F}$ exhausts the total photoabsorption cross section. Therefore, photofission has been used to study the photon absorption process [7], and $\sigma_{\gamma,F}$ has been used as a substitute for $\sigma_{\gamma,A}$, which is very difficult to measure by other methods for the case of high-Z nuclei.

The energy range available at Jefferson Lab begins in the Δ resonance region and continues up through the production of other baryon resonances. These resonances may behave quite differently inside the nuclear medium compared with the case for free nucleons. Here, the cross section can be used to study possible modifications induced by the nuclear medium on the intrinsic properties of nucleons, and the interaction and propagation of nucleons and their resonances inside nuclei (Ref. [8], and references therein).

Above the resonance region, however, the interaction between the incident photon and the target nucleus starts to resemble a hadronic process, incident photons mainly interacting with surface nucleons, while leaving the interior of the nuclear volume ''shadowed.'' The onset of this effect is an issue of current interest [9] and there are very few data available for heavy nuclei.

The microscopic mechanism governing photoabsorption is also not completely understood in the few-GeV energy region and there are also issues related to the fission process itself. Thus, by measuring the photofission cross section for heavy nuclei at these energies, we aim not only at clarifying controversial lower-energy results and checking their validity at higher photon energies, but also at extracting new physics.

II. PRESENT STATUS

A. Previous photofission measurements

For almost 50 years after the discovery of the fission phenomenon, particle-induced fission, especially by neutrons, has provided most of the available experimental information on the fission process. More recently, the well-understood electromagnetic interaction has been exploited to study induced fission reactions. Such weakly interacting probes permit the study of the photon absorption mechanism not only on the nuclear surface, but inside the nuclear volume as well. Many of the new generation of photofission measurements employed the photon-tagging technique at high-duty-cycle electron accelerators.

*Present address: Digipoint S.r.l., Corso Perrone 25/R, 16152 Genova GE, Italy.
†Deceased.

TABLE I. Previous photofission data for actinides.

Nuclei	Laboratory	E_γ (MeV)	Reference
^{238}U, ^{235}U	Bonn	120–460	[4]
^{238}U, ^{235}U	Yerevan	300–2600	[10]
^{238}U, ^{237}Np	Novosibirsk	60–240	[11]
^{238}U, ^{235}U	Mainz	50–800	[6,12]
^{238}U, ^{232}Th	Frascati	200–1200	[13,15]
^{238}U, ^{235}U	Saskatoon	60–260	[14]
^{233}U, ^{237}Np, ^{232}Th	Saskatoon	60–260	[14]

In the actinide region of the periodic table, measurements were done mostly for two of the uranium isotopes ^{238}U [4,6,10–14] and ^{235}U [4,10,12,14], spanning the energy region from 50 MeV to 2.6 GeV, as shown in Table I. Various experiments show differences up to 15% both for the case of the same isotope and between two uranium isotopes. Moreover, the Yerevan data [10], going up to 2.6 GeV, are inconclusive due to large experimental uncertainties. In addition to the uranium isotopes, measurements were done for ^{237}Np [11,14] and ^{232}Th [14,15]. Both experiments on ^{237}Np agree in measuring a substantially higher photofission cross section per nucleon for ^{237}Np than for ^{238}U. Thorium, an actinide nucleus with atomic number Z only two units less than uranium, has a fission cross section only 70% of that for uranium.

The photofission of $^{\text{nat}}$Pb has been studied only for $E_\gamma = 120–220$ MeV [16]. Additionally, data were obtained by deconvolution of inclusive electrofission data [17], but the uncertainty in the unfolding procedure makes these data less reliable. There are photofission data for Bi [18] and Au [19] in the energy range 100–300 MeV, and for both nuclei the fission cross sections are monotonically increasing functions of the incident photon energy.

To summarize, previous photofission data have been obtained up to 1.2 GeV for ^{238}U and ^{232}Th, up to 800 MeV for ^{235}U, up to 260 MeV for ^{233}U and ^{237}Np, and up to 220 MeV for $^{\text{nat}}$Pb. The present experiment overlaps with and extends the photofission measurements for all six of these nuclei up to 3.8 GeV.

B. Photofission and photofissility

One issue confronting this experiment is whether, at the energies available at Jefferson Lab, the photofission cross section $\sigma_{\gamma,F}$ for uranium and transuranic isotopes exhausts the total photoabsorption cross section $\sigma_{\gamma,A}$. If we define the *photofissility* W_F of a nucleus as the probability that this nucleus undergoes fission after absorbing a photon, then we can express W_F as the ratio

$$W_F = \frac{\sigma_{\gamma F}}{\sigma_{\gamma A}}. \tag{1}$$

For nuclei heavier than deuterium ($Z \geqslant 3$), the concept of "universal behavior" [4,20], or A-independent $\sigma_{\gamma,A}/A$, implies that, for two nuclei, the ratio of their photofissilities is given by the ratio of their photofission cross sections per nucleon

$$\frac{(W_F)_1}{(W_F)_2} = \frac{(\sigma_{\gamma F}/A)_1}{(\sigma_{\gamma F}/A)_2}. \tag{2}$$

Again, it had long been assumed that, for uranium and transuranic isotopes, $\sigma_{\gamma,F} \simeq \sigma_{\gamma,A}$ for $E_\gamma \geqslant 50$ MeV. However, this assumption had to be reconsidered after it was reported [11] that the fission cross section per nucleon for ^{237}Np was about 30% higher than that for ^{238}U up to 240 MeV. Subsequent measurements [14] corroborated these results in the same energy range. The validity of this trend up to the GeV region is not a trivial assumption. If it were true, then the photofissility of uranium would be less than unity, which invalidates the use of the photofission cross section alone to determine the total photoabsorption cross section.

Moreover, there are differences in the literature for the fission cross sections of various uranium isotopes, as shown in the previous section. As for all nuclei, one can assume that these differences are largely due to different values of the fissility parameter Z^2/A. The present experiment evaluates the differences among three uranium isotopes, neptunium, thorium, and lead, over a wide range of photon energies. This addresses the question of whether there is a Z^2/A saturation of the fission probability and whether it is photon-energy dependent.

The fissility parameter of ^{232}Th is $Z^2/A \approx 35$. Thorium lies in the transition region between the preactinide nuclei, with $Z^2/A < 35$ and high single-humped fission barriers with heights of 25–30 MeV, and heavier actinide nuclei, with $Z^2/A > 35$ and low double-humped fission barriers of 5–6 MeV. The existing data [13,14] show a fissility for ^{232}Th relative to ^{238}U slowly increasing from about 0.6 at 100 MeV to almost 0.8 at 1200 MeV. The present measurements can determine whether the fission probability of ^{232}Th relative to heavier nuclei saturates in the few-GeV energy region.

For the preactinide nuclei, such as Pb, high fission thresholds make the fissility a strong function of the excitation energy, and consequently this process is more directly related to the photoexcitation process. Recent data [16] show values of the lead fissility relative to neptunium increasing from 0.015 at 120 MeV to almost 0.035 at 220 MeV. As for thorium, we can determine the value of its relative fissility up to 3.8 GeV, and whether it becomes energy independent. Additionally, since there are recent measurements of the total photoabsorption cross section for lead up to 2.5 GeV [21], we are able to determine the absolute photofissility for lead up to this energy.

C. The photoabsorption mechanism

In the region of the Δ resonance, several sets of measurements for various nuclei ranging from lithium to uranium have been performed using different experimental techniques. For all of the nuclei studied, a resonancelike cross

section has been observed. Moreover, the cross sections scaled by the mass number have a very similar behavior, following the so-called ''universal curve.'' However, the results of different experiments vary by at least 10%.

For nuclei with A≥6, $\sigma_{\gamma,A}/A$ has an almost A-independent behavior and a shape clearly different from that of the proton. The decrease and broadening of the cross section have been explained to ~10% within the framework of the Δ-hole model [22]. But, while the Δ resonance is only slightly distorted by the nuclear medium, higher excited-nucleon states appear to be much more strongly influenced. The D_{13} and F_{15} resonances, seen clearly in the photoabsorption on the proton [23], the deuteron [24], and ^{3}He [25], are washed out in the total cross sections for A≥4 nuclei [12,21,26,8,20].

The new experimental information regarding photoabsorption obtained from the present experiment is the cross section for ^{237}Np. To the extent that $W_F \approx 1$ for ^{237}Np, its total cross section per nucleon can be compared with the bulk of photoabsorption data on other nuclei.

Above the nucleon-resonance region, the nuclear photoabsorption cross section appears to be structureless and slowly decreasing with energy relative to that of the free nucleon. This is known as ''nuclear shadowing'' [27]. This effect is generally described by considering the photon to be a superposition of a bare photon and a hadronic fluctuation with the same quantum numbers, the shadowing being produced by coherent multiple scattering of the hadronic intermediate state on different nucleons inside the nucleus. Shadowing in nuclei manifests itself as the total absorption cross section gradually evolves from purely volume absorption ($\propto A$) towards purely surface absorption ($\propto A^{2/3}$). The shadowing effect can be evaluated quantitatively by use of the expression

$$\frac{A_{\rm eff}}{A} = \frac{\sigma_{\gamma A}}{(Z\sigma_{\gamma p} + N\sigma_{\gamma n})},$$

where $A_{\rm eff}$ represents the effective number of nucleons seen by the incident photon, while $\sigma_{\gamma p}$ and $\sigma_{\gamma n}$ are the free-nucleon photoabsorption cross sections for the proton and neutron, respectively.

Earlier experiments [28,29] found values of $A_{\rm eff}/A \leq 1$ starting around 2 GeV and decreasing with increasing energy. A recent experiment [21] gives the $A_{\rm eff}$ dependence between 0.5 and 2.6 GeV for C, Al, Cu, Sn, and Pb, indicating a low-energy onset of the shadowing effect (as low as 1 GeV). Recent calculations [30] based on the vector-meson dominance (VMD) model agree with these results. Again, to the extent that $\sigma_{\gamma,F} \simeq \sigma_{\gamma,A}$ for ^{237}Np, the present experiment can also address the question of shadowing and its energy dependence up to 4 GeV.

III. EXPERIMENTAL ASPECTS

The experimental data reported in this paper were collected during the first measurements using the photon-tagging facility in Hall B at the Thomas Jefferson National Accelerator Facility (Jefferson Lab). Absolute photofission cross sections for six different nuclei (^{237}Np, ^{233}U, ^{235}U, ^{238}U, ^{232}Th, and $^{\rm nat}$Pb) were measured. One of the two fission fragments produced by the interaction of an incident photon with a target nuclei was detected using novel anode-grid parallel-plate avalanche detectors (PPADs). The PPADs were designed and built at the George Washington University Nuclear Detector Laboratory. Data for the six nuclei were collected simultaneously, facilitating a reliable comparison. Some of the initial results of this experiment have been previously reported [31].

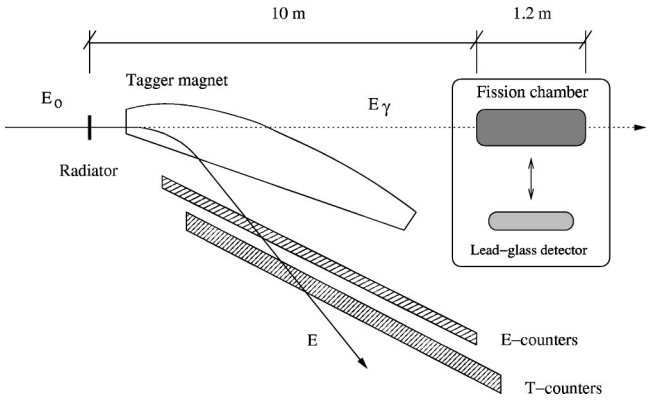

FIG. 1. Schematic view of the experimental setup used for the photofission measurements (not to scale).

The experimental setup used for the photofission measurements is shown in Fig. 1. The reaction chamber was positioned in the photon beam with the entrance window located 10 m downstream of the tagger radiator. For all of the experimental runs, the electron beam was incident on a gold radiator foil yielding $\sim 3\times 10^7$ γ/s in the energy range covered by the tagger.

A. The tagged-photon beam

The quasimonochromatic photon beam used in the experiment was produced by the photon-tagging technique. The photon-tagging system at Jefferson Lab is described in detail in Ref. [32]. The magnet geometry covers a very large dynamic range of photon energies: 20–95 % of the incident electron energy. The hodoscope, consisting of two successive planes of plastic scintillators, lies along the magnet focal plane and detects the deflected electrons (see Fig. 1). The two layers provide the position and the timing information of the scattered electrons.

The 384 counters used to determine the electron energy (*E counters*) subtend approximately constant energy intervals of 0.002 E_0. Their TDC hit spectrum reflects the shape of the bremsstrahlung spectrum, as shown in Fig. 2(a). Although many of the E counters were not fully efficient at the time when the photofission experiment took place, the counters were stable and therefore did not compromise the final results.

The 61 large overlapping timing counters (*T counters*) have approximately the same counting rates within two distinct groups, as shown in Fig. 2(b). T counters 1–19 subtend a smaller momentum range, providing a counting rate 1/3 that of T counters 20–61. The higher counting rates for T

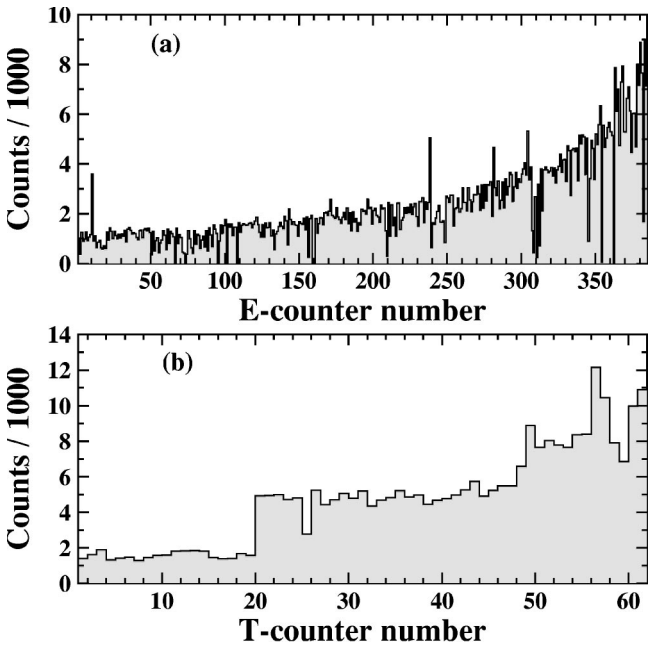

FIG. 2. Hit distributions for (a) E counters, reflecting the shape of the bremsstrahlung spectrum and (b) T counters, having approximately the same counting rates within two different groups. The higher rates at the end of the focal plane reflect the presence of beam-related background. T-channel 25 was not used for further analysis.

counters 48–61 are due to an additional background originating from a downstream source. However, requiring a coincidence between the T counters and their geometrically allowed E counters eliminates this feature.

B. The fission-fragment detectors

The applicability of parallel-plate avalanche detectors (PPADs) in detecting fission fragments has been demonstrated in several experiments [33–37]. In addition to their suitability in tagged photofission experiments, the total thickness of such counters can be kept rather small, due to the low operating gas pressure. This feature, together with the finite range of the fragments and the fact that the PPADs are almost transparent to a high-energy photon beam, allows a multiple-target-detector setup to be used. By using several targets of the same isotope, one can increase the number of counts per isotope acquired in a given amount of beam time. Furthermore, by doing simultaneous measurements for various isotopes, the relative comparisons are be more reliable.

The PPADs used in this experiment are described in detail in Refs. [37,38]. The anode plane of the PPADs consists of an array of 25-μm-diameter wires spaced 1 mm apart. Thus, only a very small fraction ($\sim$2%) of the fission fragments hit the wires, while most of them enter the active region of the detector having suffered negligible energy loss. The cathode plane is a 25-μm foil of aluminized Mylar positioned 3 mm from the anode. The operating gas is isobutane and the operating conditions are 15 Torr gas pressure and 750 V applied voltage.

TABLE II. Running conditions for photofission measurements, showing the electron beam energy and current, the range of photon energies, the corresponding tagger rate, and the number of events registered.

E_0 (MeV)	I_0 (nA)	E_γ (MeV)	Tag. rate (s^{-1})	No. events
4045.1	15	809 – 3843	2.24×10^7	13.65×10^6
1705.1	22	341 – 1620	3.26×10^7	17.34×10^6
875.9	14	175 – 832	2.72×10^7	750×10^3

Each of the fission targets consists of a thin layer ($\sim$1 mg/cm^2) of the fissionable isotope deposited on a foil substrate. For the actinide isotopes, the substrate is a 100-μm aluminum foil; for lead the substrate is a 25-μm Mylar foil. Each target was mounted in front of its own PPAD at a distance of 1.8 cm. For the actinide isotopes, two circular 4-cm-diameter collimators were used. One was placed immediately after the target, which helped to reduce the rate of α particles reaching the detector. The second collimator was placed just in front of the anode wire plane, ensuring that the geometrical acceptance of the detector was well defined. The collimators were not used for lead because the lead targets and their associated PPADs were tilted by 45° with respect to the beam line. This was done to increase the effective target thickness to gain counting statistics. To maximize the detector acceptance, each target was placed as close as possible to its associated detector. Thus, the distance between the lead foil and the anode wire grid was only 0.4 cm.

All of these target-detector combinations shared the same reaction chamber and thus the same gas pressure. This arrangement has the important advantage of enabling us to study all of the fission targets simultaneously, under exactly the same experimental conditions. The target-detector pairs were suspended from the lid of the chamber so that their centers were aligned with the entrance and exit windows of the chamber (0.5-mm-thick aluminum foils), which in turn were aligned with the photon beam line within approximately 1 mm.

C. The photofission measurements

The photofission measurements were performed at three different electron beam energies. For each of them, the beam current was chosen so that the signal-to-background ratio in the PPADs was approximately 1:1 in order to optimize the counting statistics. The electron beam and tagger parameters for the three sets of experimental runs are listed in Table II.

We used three target-detector pairs for each actinide and eight for lead. Their positions in the reaction chamber are shown in Fig. 3; the target locations are given in Table III. All of the actinide targets, with the exception of the last thorium target, were placed perpendicular to the photon beam. The thorium target in position 15, together with all of the lead targets and the Mylar one, were placed at an angle of 45° with respect to the beam line. By tilting one of the actinide targets, we established a consistency check for the geometrical acceptances of the detector in the two configu-

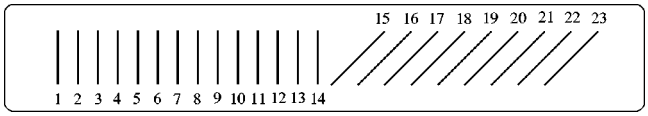

FIG. 3. Top view of the reaction chamber, showing the arrangement of the 23 target-detector pairs. The nuclear species for each of the 23 positions is given in Table III.

rations. For the lead targets, the Mylar substrate contributes a background of a few percent to the lead yield. The Mylar foil used as a ''blank'' had the same 25 μm thickness as the one used as backing for the lead targets.

D. Photon flux measurements

The ratio of tagged photons actually striking the target to the tagging electrons is called the ''tagging efficiency.'' In order to determine this ratio, we used a total-absorption lead-glass detector. Since the lead-glass detector could not handle high beam intensities, special tagging-efficiency runs were necessary. The lead-glass detector and the reaction chamber were placed parallel to the beam line on a remotely controlled moving table, which moved perpendicular to the beam line: thus we could insert either one along the beam line (see Fig. 1). For the tagging-efficiency runs, the incident electron beam current was reduced to 0.1 nA, and the lead glass was positioned along the beam line in the same position as the reaction chamber; thus the photon flux was measured at the same location as the photofission events.

IV. DATA REDUCTION AND NORMALIZATION

A. Timing calibration

In order to achieve the best coincidence time resolution between the tagger TDCs and the PPADs, several time corrections have been made. These were the timing alignment of all T-counter/PPAD combinations, the correction for the trigger time jitter, and the correction for discriminator walk.

In Figs. 4(a) and 4(b) we present the combined effect of all timing corrections. Figure 4(a) shows the raw tagged TDC spectrum for all the tagger channels and all PPADs with ^{237}Np targets, before any correction was applied (FWHM = 5 ns). Figure 4(b) shows the same spectrum after all corrections have been applied (FWHM = 1.5 ns) and illustrates that the time resolution has been much improved. Here the 2-ns RF bunch structure of the electron beam is now evident. Figure 4(c) shows the coincidence time spectrum after the accidental-coincidence background has been subtracted (see Sec. IV C).

TABLE III. Positions of the target nuclei in the reaction chamber, where No. 1 is upstream and No. 23 is downstream. They are 4 cm apart. The last column gives the total target thickness for each nucleus.

Nucleus	Position	Thickness (mg/cm^2)
^{233}U	1,6,11	1.83
^{235}U	2,7,12	2.89
^{238}U	3,8,13	4.31
^{237}Np	4,9,14	2.86
^{232}Th	5,10,15	3.71
^{nat}Pb	16–22	6.73
Mylar	23	3.56

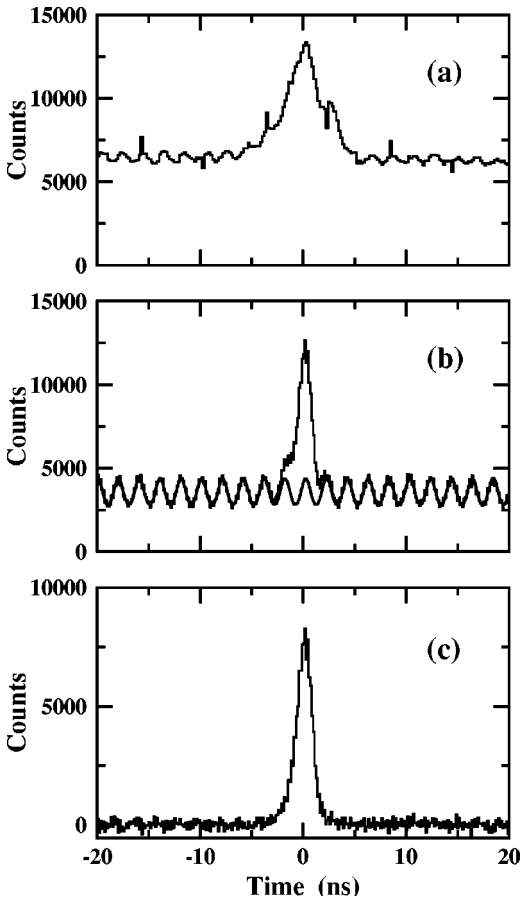

FIG. 4. Time-coincidence spectrum between the PPAD and T counter signals: (a) before applying the timing corrections and (b) before and (c) after subtraction of accidental coincidences, for all of the T channels added together.

B. Event-selection criteria

In order to determine which of the PPADs generated the experimental trigger, a count was required in both a PPAD ADC and TDC spectrum. Additionally, only those events for which only a single PPAD fired were used for further analysis. A correction of 1.5% was required to compensate for the events with higher multiplicities.

A typical PPAD ADC spectrum (Fig. 5) shows a valley between the α particles and the fission fragments. The degree of overlap between the two distributions depends on the nature of the target isotope and also on the characteristics of the particular detector. For the actinide isotopes, the yield of coincidence fission-fragment events is given by the events above a cut placed in the lowest part of the valley. A different procedure was applied for the case of lead, where the

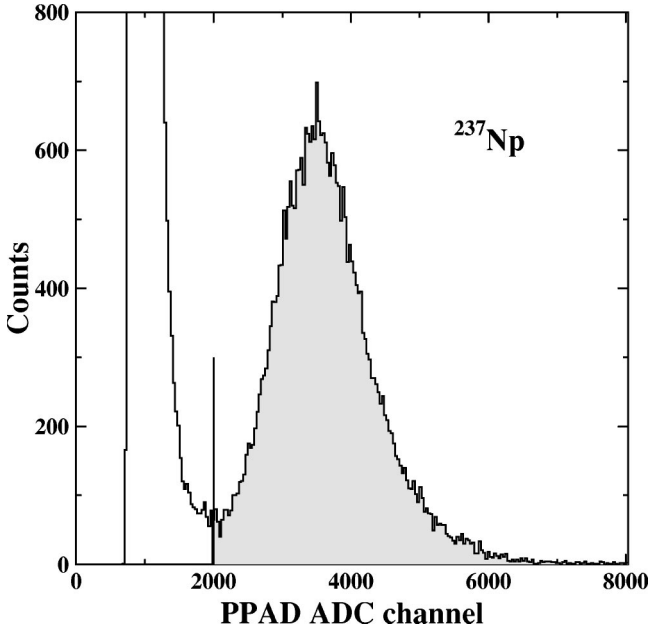

FIG. 5. Raw PPAD ADC spectrum corresponding to one of the detectors with a ^{237}Np target. The shaded area was used to determine the fission-fragment yield.

α-counting rate is high relative to the fission rate (see Sec. V A).

Each T-counter scintillator is read at both ends, referred to as left and right. Only the events which had both left and right T-counter signals present were used for analysis. The tagger time is then defined as the average of the times from the left and right ends of the scintillator, and is independent of the position where the tagged electron hit the scintillator.

The E- and the T-counter detector planes have a geometric correspondence such that electrons with appropriate trajectories can pass only through specific E- and T-counter combinations. Events which did not satisfy this geometric matching must be due to background and were not included in the analysis. Additionally, events were kept only if the time difference between the E and the T counter was within the 20-ns-wide time coincidence peak of the two. These requirements reduced significantly the background from secondary sources in the tagger focal plane, especially for T counters 48–61. Identical requirements were imposed on production and normalization runs alike.

C. Background subtraction

The coincidence peak between a PPAD signal and the associated electron detected in the tagger focal plane rests on an extended background of random coincidences due to events caused by untagged photons and by uncorrelated radioactive decay products. Because of their different levels of natural radioactivity, the background subtraction was carried out for each nucleus separately.

The random background was fitted with a function consisting of a sum of Gaussians at regular 2-ns intervals, added to a linear function, and this fit was interpolated through the region of the coincidence peak. By subtracting the random background given by the fitting function from the experimental spectrum, we obtain the spectrum shown in Fig. 4(c), where the coincidence peak is now seen to rest on essentially zero background.

D. Tagging efficiency

For the kth tagger channel, the number of photons N_γ detected by the lead-glass detector was divided by the number of electrons N_e detected in the tagger focal plane by the T counters alone (corrected, if necessary), to give the *tagging efficiency* $\epsilon_T(k)=N_\gamma(k)/N_e(k)$. The number of photons per T channel counted by the lead-glass detector is given by the integral of the lead-glass TDC spectrum after background subtraction, including the events prior to the coincidence peak (referred to as *stolen coincidences*). The number of electrons detected in the tagger focal plane was determined using the tagger T-counter scalers corrected for dead-time effects.

Again, a software coincidence between E and T counters was necessary in the data analysis to suppress beam-related background. The E counters were poorly configured for this run and had very unequal efficiencies. For the photon flux calculations we define a *combined tagging efficiency* $\epsilon_{ET}(k)=N_\gamma^{ET}(k)/N_e(k)$, where, as before, the numerator is measure by the lead-glass detector, now in coincidence with both E and T counters, while the denominator is determined by the T counters alone.

Monte Carlo simulations [39] were performed in order to further investigate how well the bremsstrahlung spectrum is reproduced in the tagger focal plane. In Fig. 6(a) we present, for one normalization run, the ratios between the measured and the calculated values of $N_\gamma(k)$ and $N_e(k)$, respectively. For the photon flux we present the spectra with and without the E-T coincidence requirement. The spectrum without E-T matching shows remarkably good agreement between data and calculation up to T channel 48. It also highlights the background present above that T channel, which is eliminated by requiring the E-T geometrical matching.

In Fig. 6(b) we show the tagging efficiency ϵ_T and the combined tagging efficiency ϵ_{ET}, determined by using T counters alone and by requirering a software E-T coincidence, respectively. The one used for the analysis includes the E-T matching. This distribution is not smooth as a function of T counter number due to beam-related background present at low photon energies (high T counter number), Møller electrons at high photon energies (low T counter number), and local problems related to particular photomultiplier tubes and their associated hardware. However, the behavior for each channel is stable in time at the 2% level, as shown in Fig. 7(a), which is a plot of the ratio between combined tagging efficiencies for two normalization runs. The tagging efficiencies used in calculating the cross sections were averages over the normalization runs available at each beam energy.

E. Tagging efficiency for the 0.9-GeV run

Unfortunately, we did not succeed in obtaining a normalization run for the 0.9-GeV data. The combined tagging efficiency in this case was deduced using the tagging efficiency

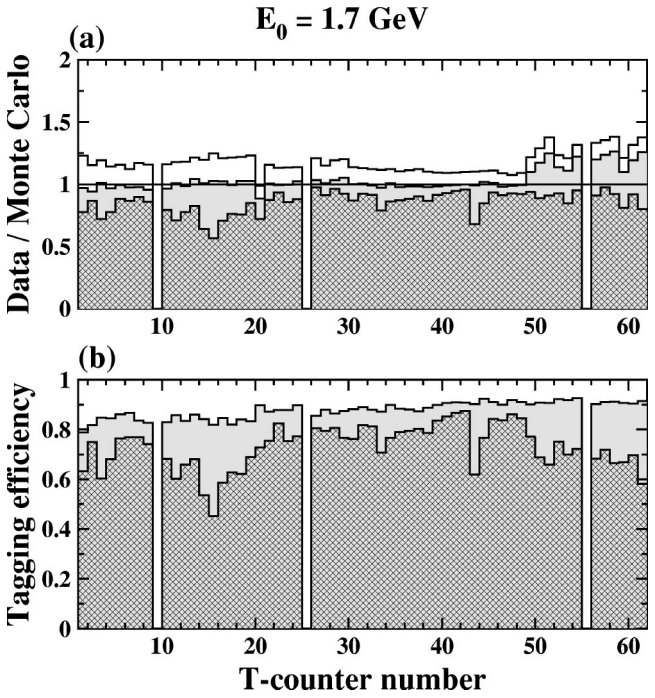

FIG. 6. (a) Ratios between data and Monte Carlo calculations: $N_\gamma(k)^{\mathrm{meas}}/N(k)^{\mathrm{MC}}$ without (shaded) and with (cross-hatched) the E-T coincidence, and $N_e(k)^{\mathrm{meas}}/N(k)^{\mathrm{MC}}$ (open). (b) Corresponding tagging efficiency ratios: $\epsilon_T(k)$ (shaded) determined by T counters alone and $\epsilon_{ET}(k)$ (cross-hatched) including a sofware E-T coincidence. Channels 9, 25, and 55 were excluded from the analysis.

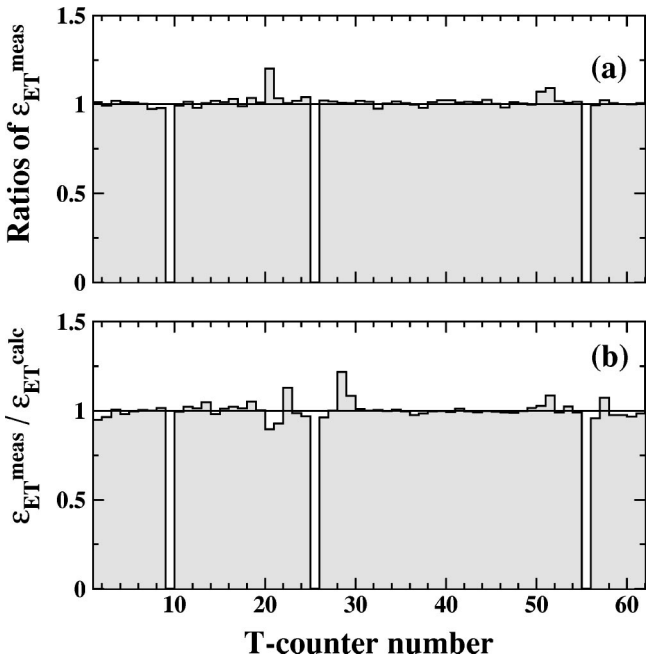

FIG. 7. (a) Ratios between combined tagging efficiencies for two 1.7-GeV runs. (b) Ratio of the measured to calculated 1.7-GeV combined tagging efficiencies.

for the 1.7-GeV data and taking into account both the change in the energy dependence across the focal plane and the change in the absolute value of the tagging efficiency. The change in the energy dependence was expressed as the ratio between counts in the random background region at two beam energies during the data runs, assuming the change is not due to the bremsstrahlung spectrum. The scaling factor was obtained by requiring good agreement of the measured cross sections in the overlap region. The average cross sections per nucleon for each nucleus were calculated for the 360–830-MeV region and a scaling factor was found for each one. The differences in the scaling factors for various nuclei are attributed to the presence of nonuniformities in the target thicknesses and to the fact that a four-times larger target area was sampled by the photon beam for the 0.9-GeV run than for the 1.7-GeV runs.

The procedure was first checked by calculating the combined tagging efficiency for the 1.7-GeV data from that of 4 GeV, and comparing it with the measured one. Figure 7(b) shows their ratio and demonstrates agreement within a few percent.

V. CROSS-SECTION DETERMINATION

For each isotope (labeled $j=1,6$) and for each tagger channel (labeled $k=1,61$), the experimental photofission cross section was calculated from the expression

$$\sigma_{\gamma F}(j,k)=\frac{Y_F(j,k)}{N_\gamma(k)}\,\frac{f_{\mathrm{sto}}(k)}{\epsilon_{\mathrm{acc}}(j)\,\epsilon_{\mathrm{det}}(j)}\,\frac{A(j)}{N_A t(j)},$$

where $Y_F(j,k)$ is the fission-fragment yield, $N_\gamma(k)$ is the tagged-photon flux, $f_{\mathrm{sto}}(k)$ is the stolen-coincidence correction, $\epsilon_{\mathrm{acc}}(j)$ is the detection acceptance, $\epsilon_{\mathrm{det}}(j)$ is the detection efficiency, $A(j)$ is the target mass number (g/mole), N_A is Avogadro's number, and $t(j)$ is the target thickness (g/cm^2).

The fission-fragment yield for each actinide isotope and each tagger T-counter channel was determined as the area under the coincidence peak after background subtraction and after a cut on the fission-fragment peak in the ADC spectrum. For the case of lead, a different technique was used (see Sec. V A).

The tagged-photon flux $N_\gamma(k)$ striking the target is determined from the expression

$$N_\gamma(k)=N_e(k)\,\epsilon_{\mathrm{tag}}(k)=N_e(k)\frac{N_\gamma(k)^{\mathrm{norm}}}{N_e(k)^{\mathrm{norm}}},$$

where the electron flux $N_e(k)$ is registered by the T-counter scalers and corrected for dead time by 2–3.5 %.

The stolen-coincidence correction $f_{\mathrm{sto}}(k)$ for the kth tagger channel was calculated from the electron rate in that channel. For a typical electron rate of $R_e(k)\simeq 0.5\times 10^6$ events/s, it is approximately 5%.

The geometrical acceptance of a target-detector combination is the fraction of the 4π solid angle in which fission fragments produced in the target can be detected by the corresponding PPAD. This effective solid angle was estimated using a Monte Carlo calculation, resulting in values of

$$\epsilon_{\mathrm{acc}}=0.385\pm 0.0036 \quad \text{(a)},$$

$$\epsilon_{\mathrm{acc}}=0.854\pm 0.0034 \quad \text{(b)},$$

where (a) stands for the combinations which include a collimator and are placed perpendicular to the beam line and (b) for those without collimator and tilted by 45° with respect to the beam line.

At our operating conditions (15 Torr and 750 V), the PPADs have a very high efficiency for detecting fission fragments. The small inefficiency is due to the fact that the anode wire plane is not completely transparent to fission fragments and has values of

$$\epsilon_{\mathrm{det}} = 0.975 \quad \text{(a)},$$

$$\epsilon_{\mathrm{det}} = 0.948 \quad \text{(b)},$$

where (a) and (b) have the same meaning as above.

Since all of the actinide fission targets have natural α activity, their thicknesses and isotopic compositions were determined by measuring their α-activity rates and energy spectra. The measurements were done, using a silicon surface-barrier detector, to an accuracy of $\approx 3\%$. These measurements are described in detail in Ref. [40]. The thickness of $^{\mathrm{nat}}$Pb deposited on the Mylar substrate was given by the manufacturer. The total thickness for each nuclear species is given in Table III.

For each incident beam energy, each tagger T-counter channel covers a given fraction of the energy range of the incident photon beam. These fractions are calculated knowing the size of the detectors and their positions in the magentic field [39]. The corresponding photon energy for a given tagger channel is taken to be the middle of the energy range covered by each T counter.

A. Special cases

A non-negligible amount of ^{238}U was present in the ^{235}U and ^{233}U targets. Consequently, the measured cross sections for both ^{235}U and ^{233}U include a contribution from the ^{238}U contamination, and had to be corrected accordingly. The resulting cross sections for ^{235}U and ^{233}U were determined from

$$\sigma_i = \left(1 + \frac{A_i}{A_{238}} \frac{t_{238}}{t_i}\right) \sigma_i^{\mathrm{meas}} - \frac{A_i}{A_{238}} \frac{t_{238}}{t_i} \sigma_{238}^{\mathrm{meas}}, \qquad (3)$$

where the index i signifies either ^{235}U or ^{233}U, σ and σ^{meas} are the corrected and the measured cross sections, t and A are the thicknesses and mass numbers, and $\sigma_{238}^{\mathrm{meas}}$ is the cross section for ^{238}U obtained in the present experiment.

The $^{\mathrm{nat}}$Pb yields needed to be obtained differently from the actinide targets due to the small size of the lead photofission cross section. Here, the contributions of coincident α particles [from the (γ,α) reaction] and of the Mylar substrate are non-negligible. The coincidence peak in the TDC spectrum therefore includes, besides fission events, both Pb(γ,α) events and events coming from the Mylar backing. Here, the reaction yield was obtained by subtracting from the PPAD ADC spectra that of the lead-free backing. The TDC spectra were used only to evaluate the contribution from the random background.

TABLE IV. Systematic uncertainties due to tagging efficiency, target thickness, and the combined uncertainties for the actinide and lead targets, for the 4.0-GeV and 1.7-GeV data.

$\delta\sigma^{sys}$	4.0 GeV		1.7 GeV	
Tagging efficiency	$\sim 4\%$		$\sim 2\%$	
	actinides	lead	actinides	lead
Target thickness	4.7%	3.2%	4.4%	2.9%
Total	6.2%	5.1%	4.8%	3.5%

B. Systematic uncertainties

The systematic uncertainty $\delta\sigma^{\mathrm{sys}}$ for the cross section is the combined effect of uncertainties in determining the fission-fragment yield, the tagged-photon flux, the PPAD geometrical acceptance, and the target thickness.

The uncertainty in determining the fission-fragment yield is in turn due to uncertainties introduced by the cuts used as event-selection criteria: the ADC threshold, the left-right cut, and the E-T matching. The choice of the ADC threshold introduces a variation of less than 1% of the total yield. The last two cuts are applied both to the data and to the normalization runs, so that the fraction of counts excluded from the fission yield is the same as that excluded from the photon flux used for normalization, resulting in an insignificant overall uncertainty.

For each energy, the tagging efficiency was calculated for each energy channel as an average over all normalization runs. The differences between individual runs give an estimate of the systematic uncertainty associated with the tagging efficiency. These differences, averaged over the tagger focal plane, are listed in Table IV for two beam energies.

As a consistency check of the absolute normalization for different data sets, the cross sections obtained with at $E_0 = 4.0$ GeV and $E_0 = 1.7$ GeV were compared in their overlap region, which extends from 850 MeV to 1.6 GeV. Figure 8 shows the photofission cross sections obtained with the two beam energies for ^{237}Np. For each of the six nuclei, the agreement between the two sets of data is excellent (to within 2%).

The detector acceptance was calculated numerically. The positions of various detectors in the chamber, as well as small variations in relative positions within the target-detector assembly, result in acceptance differences smaller than 1%.

The actinide target thicknesses were measured to an accuracy of about 3%. For the lead foils, the manufacturer gave an uncertainty of 10%. However, the cross sections per detector averaged over the tagger focal plane show variations larger than 3% for the actinides but much smaller than 10% for lead.

For each target nucleus and for each incident electron energy, the cross sections were obtained by combining the data from the PPADs for the same nucleus. Due to limited statistics, the variations among different target-detector combinations were able to be evaluated only by combining the data from all 61 T channels.

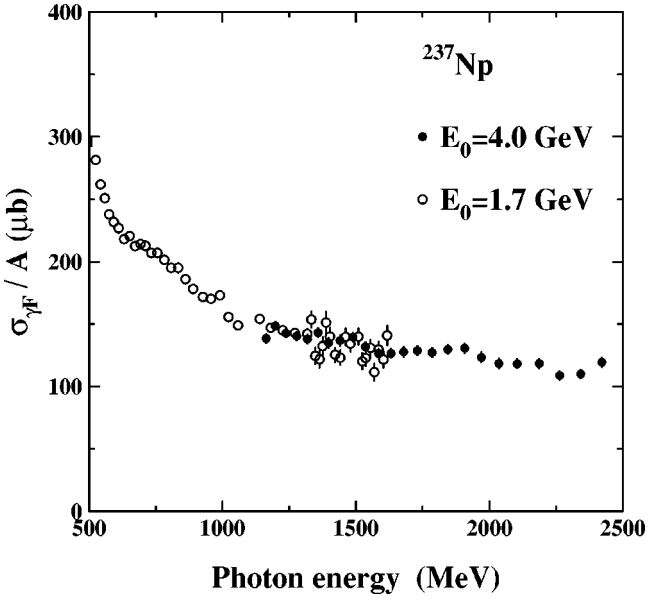

FIG. 8. Photofission cross section per nucleon for ^{237}Np, showing the overlap region between data at $E_0=4.0$ GeV (●) and $E_0=1.7$ GeV (○).

Among the actinides, the highest variations (≈5–19 %) are exhibited by ^{232}Th and the lowest ones (≈1–5 %) by ^{238}U. For the actinide nuclei, the ratios of individual target cross sections to average cross sections per nucleus are approximately the same for the two incident beam energies. This implies that the differences within one nucleus are most probably due to target-thickness variations, and they represent the main source of systematic uncertainty. All of the actinide data were considered to be a set of 12 data points, and since for each actinide we had three targets, the deviation from the mean values per actinide nucleus yielded the assigned uncertainty. The values attributed as systematic uncertainties due to target thickness are summarized in Table IV, which contains also the estimated total systematic uncertainties for the actinides and for lead for the two electron beam energies of 4.0 and 1.7 GeV, respectively. The uncertainties for the 1.7-GeV data are smaller, consistent with the fact that the beam-spot size was much larger for these runs.

VI. RESULTS

A. Absolute photofission cross sections

Photofission data have been obtained for photon energies from 0.17 to 3.84 GeV, using three incident electron energies. The good agreement in the overlap region between the two higher-energy bites was presented above. Data in the overlap regions for two incident electron energies were combined by taking the appropriately weighted average. Data were then rebinned in equal-energy bins. The bin sizes were chosen taking into account both the shape of the cross section as a function of incident photon energy and the size of the statistical uncertainties. Thus, in the region of the Δ resonance, where the cross section varies rapidly with energy, the bins are narrow (20 MeV). Above 1 GeV, the cross section is smaller and almost energy independent, so the bins are wider (150 MeV).

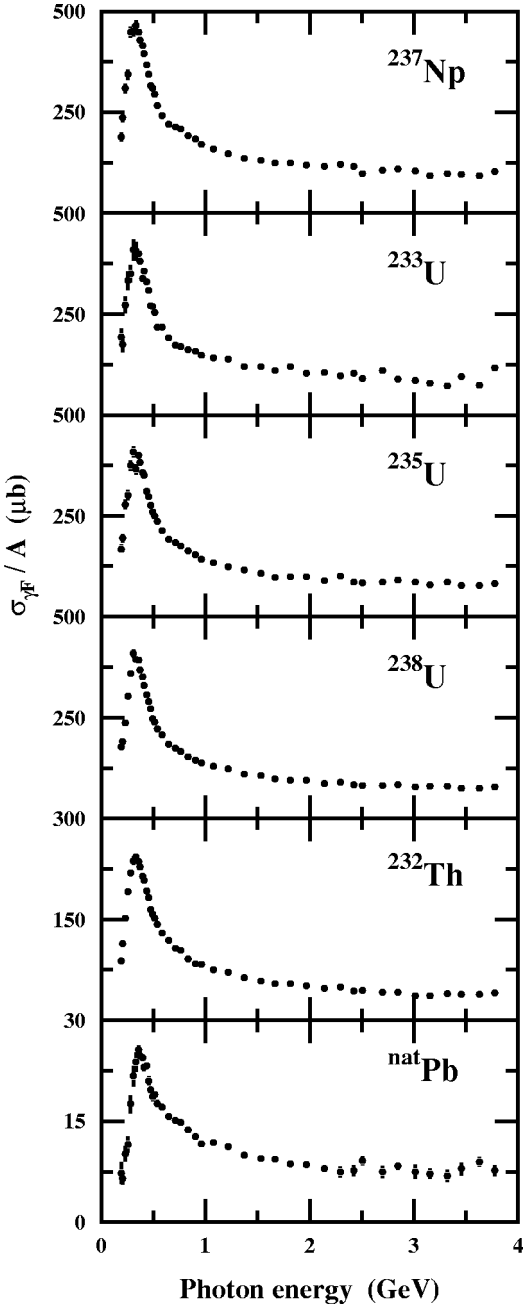

FIG. 9. Absolute photofission cross sections per nucleon as a function of the incident photon energy for ^{237}Np, ^{233}U, ^{235}U, ^{238}U, ^{232}Th, and ^{nat}Pb.

Figure 9 shows our results for the absolute photofission cross sections per nucleon $\sigma_{\gamma F}/A$, as a function of the incident photon energy, for all six nuclei. The error bars reflect the statistical uncertainties only. The values for the photon energies, fission cross sections, and associated statistical uncertainties are presented in Table V.

In Fig. 9, data for neptunium and the three uranium isotopes are shown with the same scale on the vertical axis. The photofission cross section per nucleon for ^{237}Np has the highest absolute value, significantly higher than that for ^{238}U. One can also notice small differences between the three uranium isotopes; the cross section per nucleon for

TABLE V. Table of photon energies, absolute photofission cross sections per nucleon, and associated statistical uncertainties for ^{237}Np, ^{233}U, ^{235}U, ^{238}U, ^{232}Th, and ^{nat}Pb.

	$\sigma_{\gamma,F}$/A (μb/nucleon)					
E_γ (MeV)	^{237}Np	^{233}U	^{235}U	^{238}U	^{232}Th	^{nat}Pb
193	188.2±11.4	192.9±20.6	167.2±10.7	177.4±8.2	88.4±4.6	7.3±1.6
208	237.0±11.4	174.5±20.0	194.4±10.6	191.4±8.1	113.8±4.7	6.5±0.9
235	309.2±12.2	272.8±21.3	278.6±11.8	237.8±8.7	151.9±5.1	10.2±1.2
258	343.6±12.5	332.6±22.5	301.5±11.9	303.0±9.2	191.6±5.5	11.5±1.2
282	448.2±13.2	350.0±22.2	375.0±12.2	358.8±9.4	219.1±5.6	17.6±1.3
307	452.4±14.6	408.6±25.2	408.5±13.8	408.3±10.7	237.3±6.4	21.7±1.6
337	464.3±13.4	405.7±23.1	365.0±12.4	394.4±9.8	243.3±5.9	23.8±1.4
361	449.1±5.0	400.0±9.2	400.2±4.9	393.3±3.6	236.3±2.2	25.6±0.6
376	429.2±3.6	381.9±6.7	382.0±3.5	368.0±2.6	228.0±1.6	24.8±0.5
397	415.1±3.6	337.9±6.5	357.5±3.5	350.8±2.5	214.5±1.6	24.5±0.5
414	395.3±4.6	357.1±8.6	351.0±4.5	329.0±3.2	208.6±2.0	23.1±0.6
440	367.4±4.6	330.1±8.4	311.0±4.4	306.9±3.2	192.3±2.0	23.2±0.6
454	345.0±4.8	308.4±9.0	297.6±4.7	289.3±3.4	182.4±2.1	21.0±0.7
474	316.4±3.4	271.0±6.2	275.7±3.3	271.9±2.4	164.3±1.5	19.7±0.5
494	310.0±4.9	269.4±9.0	259.2±4.7	246.9±3.4	157.8±2.1	18.7±0.7
516	294.3±2.9	254.0±5.4	250.5±2.8	238.2±2.0	151.3±1.3	19.0±0.4
543	267.1±4.2	217.8±7.8	236.9±4.1	221.4±2.9	142.3±1.8	17.5±0.6
583	241.3±2.3	217.9±4.2	213.6±2.2	206.6±1.6	130.1±1.0	17.1±0.3
650	220.1±2.4	191.9±4.5	191.4±2.3	184.5±1.6	119.3±1.0	15.7±0.3
715	213.7±1.6	172.4±2.9	183.5±1.5	174.1±1.1	107.3±0.6	15.1±0.2
765	208.7±2.5	169.6±5.8	174.9±2.4	165.2±1.7	104.0±1.0	14.9±0.4
837	191.4±1.5	162.1±2.8	163.2±1.4	153.0±1.0	91.5±0.5	13.7±0.2
908	183.2±2.2	158.5±4.2	153.1±2.1	144.0±1.5	83.9±0.7	12.7±0.3
965	171.3±1.9	148.9±3.6	142.9±1.8	138.2±1.3	82.9±0.6	11.6±0.3
1077	159.8±1.7	140.8±3.2	134.2±1.6	130.4±1.1	75.0±0.5	11.8±0.2
1219	147.3±1.5	137.4±2.8	124.3±1.4	122.8±1.0	71.0±0.4	11.2±0.2
1372	136.7±1.6	119.6±3.1	116.2±1.6	110.5±1.1	63.7±0.5	9.9±0.3
1531	130.6±1.8	120.5±3.4	108.1±1.7	106.2±1.2	58.6±0.5	9.4±0.3
1670	124.9±2.3	109.6±4.4	96.9± 2.2	98.9±1.6	54.6±0.6	9.4±0.3
1815	124.3±3.1	119.3±5.9	100.0±2.9	95.2±2.1	53.9±0.7	8.7±0.5
1972	120.2±2.6	104.2±5.0	98.7±2.5	94.1±1.8	51.5±0.6	8.5±0.5
2143	115.3±3.0	105.1±5.7	89.0±2.8	86.8±2.0	47.5±0.7	8.0±0.6
2300	120.3±3.3	96.1±6.3	101.5±3.2	90.7±2.2	49.3±0.8	7.5±0.8
2422	115.3±4.5	102.8±8.5	86.8±4.2	83.4±3.0	43.5±1.0	7.7±0.8
2509	97.5±4.0	90.4±7.5	83.7±3.8	81.4±2.7	44.9±0.9	9.1±0.6
2698	105.5±4.4	110.2±8.4	86.1±4.1	81.3±2.9	41.2±1.0	7.4±0.9
2851	108.7±3.1	88.6±5.9	90.2±3.0	83.8±2.1	41.9±0.7	8.4±0.6
3013	104.9±4.2	85.8±8.0	85.2±4.0	78.5±2.8	36.2±0.9	7.5±1.0
3159	92.5±3.3	79.5±6.3	79.3±3.2	80.2±2.2	36.5±0.8	7.2±0.7
3322	97.8±4.2	72.2±7.9	85.5±4.0	79.7±2.8	39.4±1.0	6.9±0.9
3459	95.9±4.5	95.7±8.6	77.9±4.3	74.6±3.0	38.7±1.0	7.9±0.9
3629	93.4±4.0	74.2±7.6	77.3±3.8	74.5±2.6	38.1±0.9	9.0±0.7
3779	102.5±4.3	117.1±8.2	82.0±4.0	77.7±2.8	40.1±1.0	7.7±0.8

^{233}U is higher than that for ^{235}U, which in turn is higher than that for ^{238}U. The cross section for ^{232}Th is markedly lower than the other actinides, as expected from previous measurements [15,14]. The cross section for ^{nat}Pb is about an order of magnitude lower than that for thorium.

The energy dependence for all of these cross sections is similar. The Δ resonance is clearly seen, and has about the same position and width for each of the actinide isotopes. As expected from previous data, the present photofission cross sections exhibit no prominent resonance structure above the

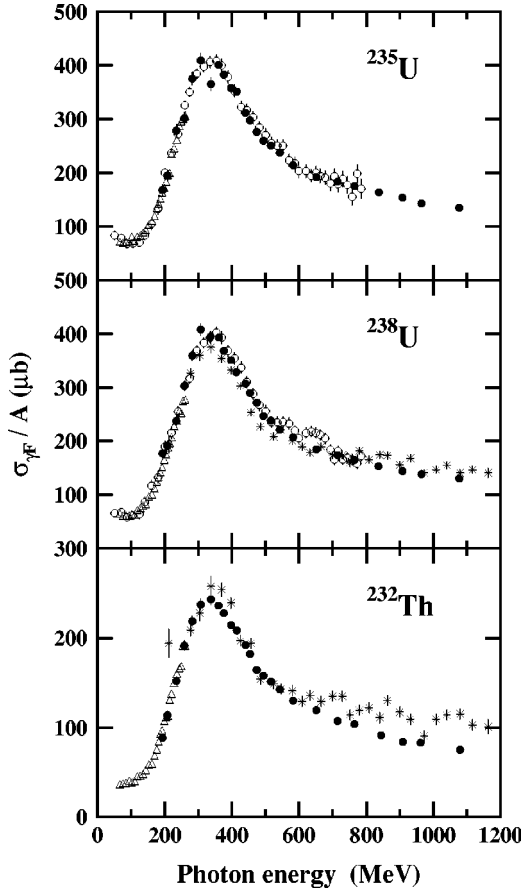

FIG. 10. Comparison of our absolute photofission cross sections per nucleon for ^{235}U, ^{238}U, and ^{232}Th with previous photofission data from Refs. [14] (△), [12] (○), and [13,15] (*).

Δ resonance, and they slowly decrease with increasing photon energy. However, there appears to be an enhancement to the cross section in the region of higher nucleon resonances (500–900 MeV).

B. Comparison with previous data

(a) *Comparison with previous photofission data*. The previously existing photofission data for the six nuclei are summarized in Sec. II A. Figure 10 shows a comparison of our data for ^{235}U, ^{238}U, and ^{232}Th, with the previous photofission data up to 1.2 GeV. The present data are in good agreement at low energies with the data from Ref. [14] which in turn agrees with the data from Ref. [11]. The ^{238}U data from the present measurement agree well with the average of the Mainz [12] and the Frascati [13] data from the Δ-resonance region up to about 800 MeV. However, the agreement is not as good between the present ^{232}Th data and the Frascati [15] data.

(b) *Comparison with photoabsorption data on the proton*. In Fig. 11 we present our photofission data for ^{237}Np together with a fit to the available photoabsorption data on the proton from Refs. [23–25]. In the region of the Δ resonance our measurements are consistent with previous (γ,A) results in showing a broadening of the Δ peak inside nuclei, compared with that of the proton. This phenomenon has been

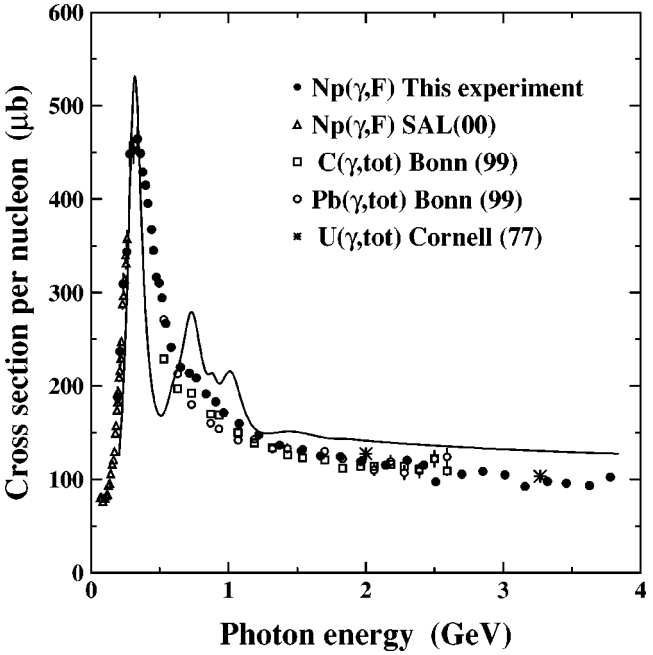

FIG. 11. Photofission cross sections per nucleon for ^{237}Np, compared with previous photoabsorption data for Pb (○) and C (□) [21] and for ^{238}U (*) [29]. A fit to the photoabsorption data for the proton [41] is also shown.

seen experimentally for several nuclei, and has been explained theoretically using the Δ-hole model [22]. The higher D_{13} and F_{15} resonances, clearly seen in the photoabsorption cross section for the proton (and for the deuteron), are not observed as prominent peaks in our photofission cross sections, as expected from previous data, but could perhaps account for the aforementioned enhancement in the 500–900 MeV region.

(c) *Comparison with photoabsorption data on other nuclei*. The most recent photoabsorption data on C and Pb [21] are also shown in Fig. 11, together with our highest photofission cross section, $\sigma_{\gamma F}$ for ^{237}Np. Above 1 GeV there is good agreement among these data sets. Thus, the photofission cross section for ^{237}Np appears to exhaust the total photoabsorption cross section almost completely. This statement will be reinforced by results presented in following sections. Second, since there is not much variation in the photoabsorption cross sections per nucleon from $A=12$ to $A=237$, we can infer that the concept of ''universal behavior'' is confirmed approximately, if not in fine detail.

A more comprehensive comparison is attempted in Fig. 12, in which we present cross-section bands representing the photofission data for ^{237}Np, ^{238}U, and ^{232}Th and the existing Pb photoabsorption data [8,21,28,42]. The photofission data sets include the present data as well as previous data from Refs. [11–15]. Both $\sigma_{\gamma F}$ and $\sigma_{\gamma A}$ data were fitted using a modified Breit-Wigner formula

$$f(x)=a+\frac{bx^c}{(x-d)^2+e}.$$

The data used for the fit and the corresponding fitted func-

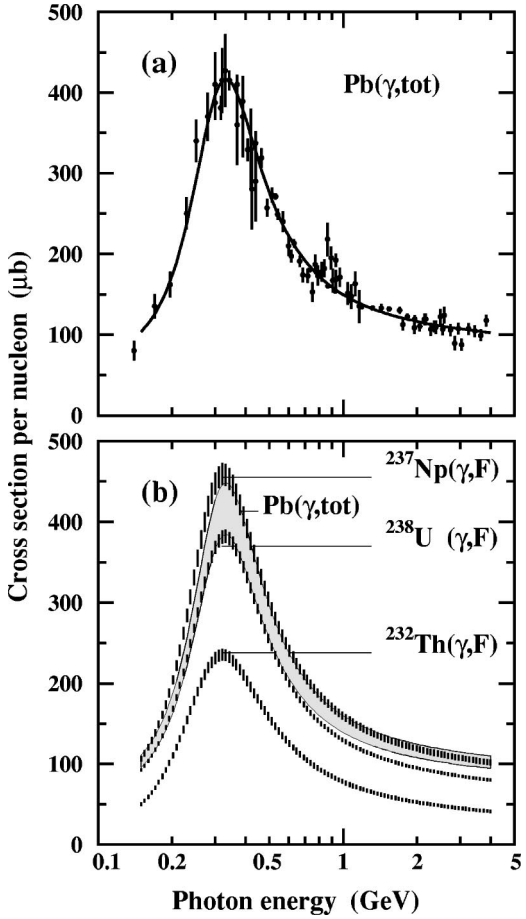

FIG. 12. (a) Fit to the existing photoabsorption data for Pb. (b) Comparison of photofission cross sections per nucleon for ^{237}Np, ^{238}U, and ^{232}Th (bar bands) with previous photoabsorption data on Pb (gray band). The bands represent fits to the existing data (see text).

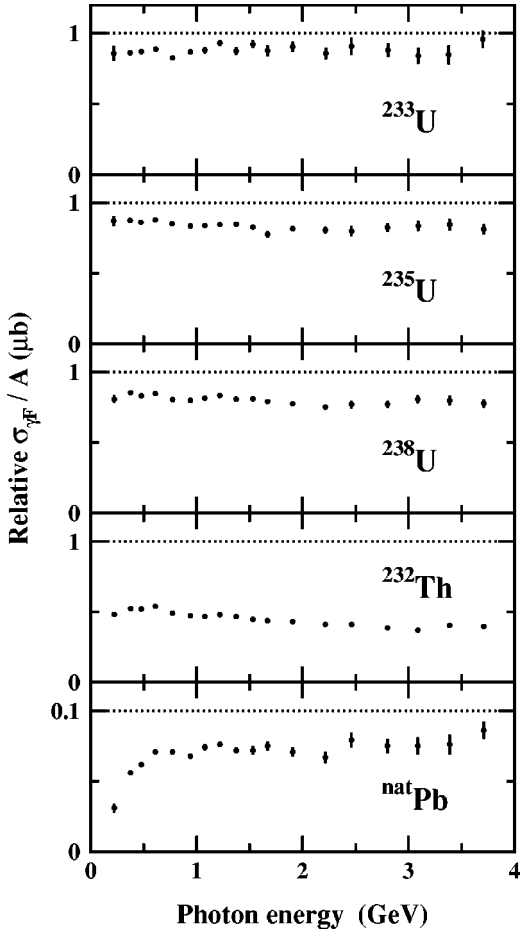

FIG. 13. Photofission cross sections per nucleon for ^{233}U, ^{235}U, ^{238}U, ^{232}Th, and ^{nat}Pb relative to ^{237}Np as a function of the incident photon energy. Only statistical uncertainties are shown, while systematic uncertainties are 6.6% for the actinides and 5.7% for lead.

tions for Pb are shown in Fig. 12(a). The band widths in Fig. 12(b) represent the uncertainties in the fits. The energy scale is logarithmic, for clarity at the lower energies. We note that the low-energy data on Pb [42] should be regarded as a lower limit since it includes only (γ,xn) cross sections, where $x \geqslant 2$, and hence does not include the other photohadron channels, such as the (γ,n), (γ,p), (γ,α), (γ,pn), or $(\gamma,\alpha n)$ channels. One can see that $\sigma_{\gamma F}/A$ for ^{237}Np is a few percent higher than $\sigma_{\gamma A}/A$ for Pb only below the Δ peak, and is in very good agreement at higher energies, indicating again that $\sigma_{\gamma F} \simeq \sigma_{\gamma A}$ for ^{237}Np.

VII. DISCUSSION

A. Photofission cross sections relative to ^{237}Np

Using the highest cross section as a reference, namely, that for ^{237}Np, we show in Fig. 13 the relative photofission cross sections per nucleon as a function of the incident photon energy. The error bars reflect the statistical uncertainties only. Because the uncertainty in the photon flux cancels, the systematic uncertainties in the cross-section ratios are dominated by the uncertainties in the respective target thicknesses. This leads to a total systematic uncertainty of 6.6% for the actinides and 5.7% for lead.

In Fig. 13 one can see that the probability for ^{238}U to undergo fission is about 20% *smaller* than that for ^{237}Np. This confirms, and extends to higher photon energies, the previous lower-energy measurements at Novosibirsk [11] and SAL [14]. The other two uranium isotopes also have fissilities lower than ^{237}Np (about 85% for ^{235}U and slightly higher for ^{233}U). Since all three uranium isotopes undergo fission with a lower probability than Np, we can conclude that our results contradict the assumption that, over this entire energy range, any of these uranium isotopes has a photofissility of 100%.

For the actinide isotopes, and for Pb above 1 GeV, the energy dependence of the relative cross sections appears to be almost flat (see Fig. 13). For Pb, the fissility relative to ^{237}Np increases rapidly below 1 GeV, then seems to be slowly reaching an asymptotic value of $\sim$0.075 towards 4 GeV. However, the fissility for ^{232}Th, which fissions with about half the probability of ^{237}Np, seems to decrease slowly as the energy increases above $\sim$500 MeV.

The almost constant energy dependence of the relative photofission cross sections suggests that a common mecha-

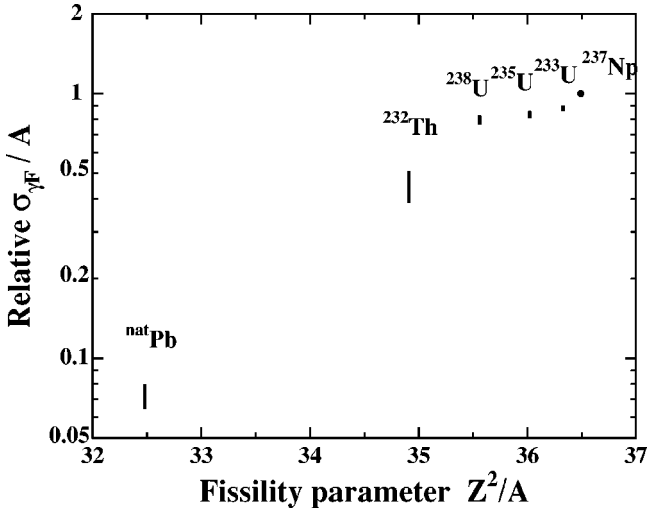

FIG. 14. Photofission cross sections per nucleon for ^{233}U, ^{235}U, ^{238}U, ^{232}Th, and ^{nat}Pb relative to ^{237}Np, as a function of the fissility parameter Z^2/A.

nism is responsible for the photofission process in all of these nuclei over a large energy range. This suggests in turn that the two-step cascade-evaporation model [43] used to explain the fission process at intermediate energies (up to about 1 GeV) may also be valid in the 1–4 GeV region. This model is discussed at length in Ref. [38], and is the subject of a forthcoming paper [44].

Using the liquid-drop model, Bohr and Wheeler [45] defined a *fissility parameter x* as half the ratio of the Coulomb energy $E_c(0)$ to the surface energy $E_s(0)$ of an undeformed nucleus of radius R_0

$$x = \frac{E_c(0)}{2E_s(0)} \propto \frac{Z^2/R_0}{R_0^2}.$$

By fitting experimental nuclear masses and yields, this parameter can be approximated as $x \simeq Z^2/50A$. The parameter x determines the probability of a nucleus to fission spontaneously. Detailed estimates of these transition rates have to account for quantum-mechanical barrier penetration and for the permanent equilibrium deformation of nuclei in the region around uranium. In the following discussion, we will refer to the ratio Z^2/A as the fissility parameter.

Figure 14 depicts these relative cross sections as a function of the fissility parameter Z^2/A. The vertical bars represent the range spanned by the relative cross sections over the energy range of the present experiment. The relative fissilities follow a monotonically increasing curve, which seems to approach an asymptote, lending further credence to the assertion that $\sigma_{\gamma F} \simeq \sigma_{\gamma A}$ for ^{237}Np.

B. Integrated cross section

Figure 15 shows the integrated cross section per nucleon $\sigma^{\rm int}/A$ for ^{237}Np and that for the corresponding sum of protons and neutrons, obtained as

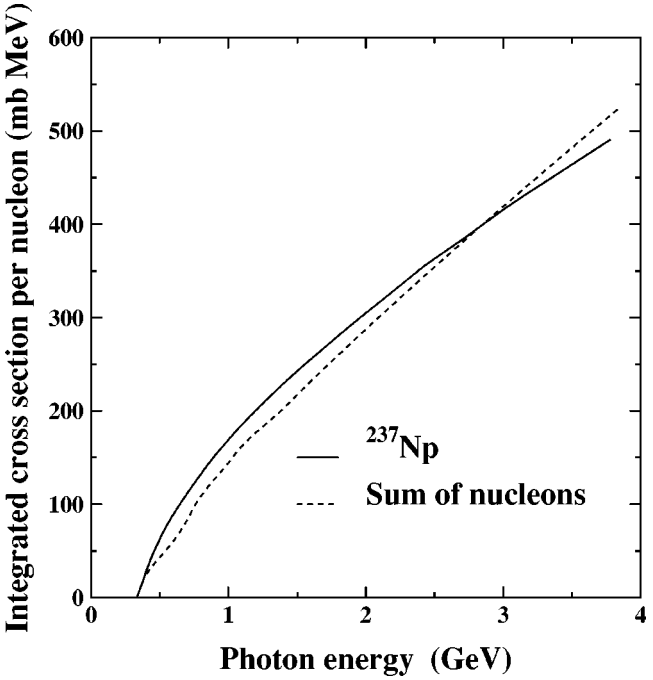

FIG. 15. Integrated cross sections per nucleon for ^{237}Np (solid line) and the sum of protons and neutrons (dashed line).

$$\frac{\sigma^{\rm int}(E_\gamma)}{A} = \int_{E_0}^{E_f} \frac{\sigma(E_\gamma)}{A} dE_\gamma,$$

where $E_0 = 330$ MeV and $E_f = 3.8$ GeV. For ^{237}Np, the present photofission data were used. For the proton and neutron, the integration was done using recent fits [41] to the photoabsorption data [23,24]. For both curves, the starting point for integration was at the peak of the Δ resonance to minimize contributions from low-energy collective effects.

If the cross section for ^{237}Np were simply that for a collection of free nucleons with Fermi momentum, one would expect a convergence of their integrals around 1.2–1.5 GeV, where both cross sections cease to display resonant structure. However, we see that there is significantly more strength in the ^{237}Np integral, indicating that there still are collective contributions well above the Δ peak, where the wavelength is of the order of the nucleon radius. The ^{237}Np integral increases less rapidly, however, and by about 2.5 GeV, the integrated photofission cross section per nucleon becomes lower for ^{237}Np than for the corresponding sum of free nucleons. This may be due partly to the onset of the shadowing effect, as discussed in the next section. However, there is also the possibility that the dynamics of the fission process may lead to a reduced fissility at high photon energy [44].

C. Shadowing

Figure 16 shows the ratios of the photofission cross sections for ^{237}Np, ^{238}U, and ^{232}Th and the corresponding cross sections for the sum of the protons and neutrons [23,24] in each of these nuclei. The photoabsorption cross section for the neutron was deduced from those for the proton and deu-

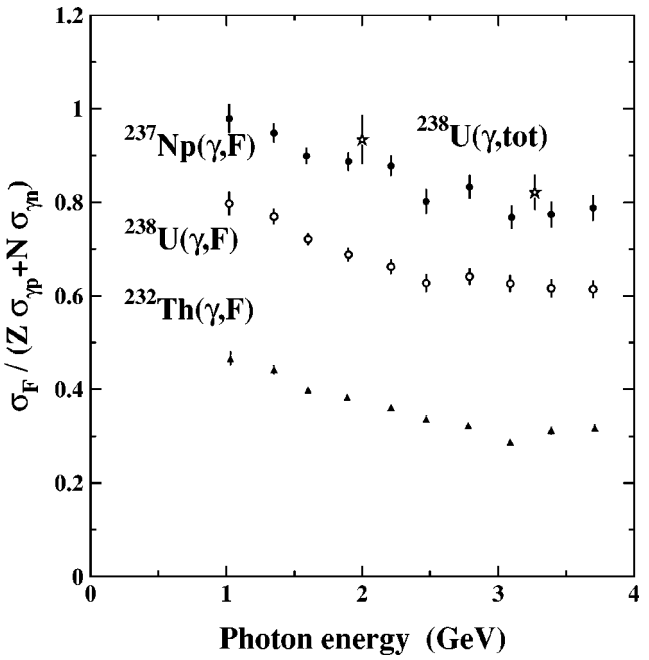

FIG. 16. Ratio of the photofission cross sections for ^{237}Np, ^{238}U, and ^{232}Th and the corresponding total cross sections for the sum of the protons and neutrons [23,24] in each of these nuclei. Two data points (open stars) for the total photoabsorption cross section for ^{238}U [29] are shown for comparison.

teron [23,24]. Two data points for the photoabsorption cross section $\sigma_{\gamma A}$ for ^{238}U [29] are shown for comparison.

We have seen that $\sigma_{\gamma F}$ is smaller than $\sigma_{\gamma A}$ for the three uranium isotopes, for Th and for Pb. Thus, we cannot use the photofission cross section to measure the shadowing effect, except perhaps for the case of ^{237}Np, if we assume that its photofission probability is close to unity, as suggested by Figs. 11, 12, and 14. Under this assumption, we observe in Fig. 16 that the onset of shadowing occurs below 1.5 GeV, and its magnitude is such that $A_{\rm eff}/A$ decreases to about 80% at 3.5 GeV, as shown in Fig. 16. It is also clear that $\sigma_{\gamma F}$ for ^{238}U is much less than $\sigma_{\gamma A}$ while $\sigma_{\gamma F}$ for ^{237}Np is not. While the slopes of the ^{237}Np photofission and the ^{238}U photoabsorption data appear to be consistent, the ^{237}Np photofission data are $\approx 5\%$ below the ^{238}U photoabsorption data, indicating that W_F for ^{237}Np is probably somewhat less than unity.

An estimate of the shadowing for the other five nuclei in addition to ^{237}Np can be obtained if we estimate their total absorption cross sections. If, again, we assume that the fissility W_F of ^{237}Np is close to unity, then the fissilities for the other nuclei are given by their fission cross sections per nucleon relative to that of ^{237}Np [see Eq. (2)]. The averages of the fissilities over the entire energy range were calculated, and then the photoabsorption cross sections were estimated by the ratios of the photofission cross sections and the corresponding average fissilities. $A_{\rm eff}$ was then calculated, and the results are shown in Fig. 17. Except for ^{232}Th, the other five nuclei show a very similar behavior, with $A_{\rm eff}/A$ values of approximately 0.8 at 4 GeV, while for ^{232}Th this value is only about 0.65.

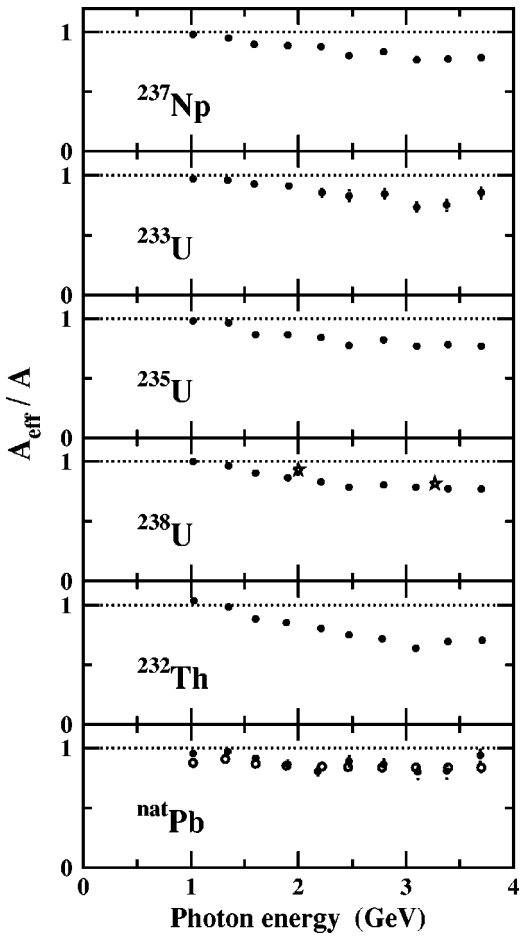

FIG. 17. Estimate of the effective relative number of nucleons seen by the incident photon for the six nuclei studied (see text for details). The open stars for ^{238}U are the photoabsorption data of Ref. [29]. The open circles for Pb are obtained by using the fit to the photoabsorption data shown in Fig. 12.

VIII. SUMMARY AND CONCLUSIONS

We have performed simultaneous measurements of the total photofission cross sections $\sigma_{\gamma F}$ for five actinide nuclei (^{237}Np, ^{233}U, ^{235}U, ^{238}U, and ^{232}Th), and for one preactinide nucleus ($^{\rm nat}$Pb) using tagged photons of energy $E_\gamma = 0.17$–3.84 GeV. Our results have a statistical uncertainty of $\sim 3\%$ (varying from 1% to 6% across the energy range), and a systematic uncertainty of $3.5-6.2\%$ (depending on the nucleus and the energy).

From our results for the absolute photofission cross sections per nucleon and from their comparison with other data, we can draw several conclusions. First, by comparing the ^{237}Np photofission cross section per nucleon with previous photoabsorption data on other nuclei, we see that the ^{237}Np photofissility is close, if not equal, to unity and that the concept of ''universal behavior'' is approximately confirmed. Second, the same comparison between fission and absorption for the other actinide nuclei shows that their fissilities are less than unity, and therefore that their fission cross sections are substantially lower than their absorption cross sections. Thus, contrary to previous belief, the photofission cross section alone cannot be used as a substitute for the photoabsorp-

tion cross section for these nuclei, even for the case of uranium. Third, the nuclear-medium modification of the Δ resonance produces, as expected, a lower and broader peak than is the case for the proton and the deuteron. Furthermore, the D_{13} and F_{15} resonances are not observed explicitly in heavy nuclei, again as expected. However, there is a slight but clear enhancement of the cross sections between about 0.5 and 1 GeV. Finally, above the resonance region, the fission cross sections decrease slowly with energy and, if we assume that the fission probability for ^{237}Np is close to 100%, we can infer a shadowing effect starting below 1.5 GeV and slowly becoming more important with increasing energy.

The photofission cross sections relative to ^{237}Np yield additional information. The nearly energy-independent behavior of the relative probability with which these heavy nuclei undergo fission indicates that a common mechanism is responsible for the photofission process, independent of whether the photon is in the few-GeV or hundred-MeV region. The relative cross sections as a function of Z^2/A seem to be approaching an asymptote. This is consistent with the assertion that the fissility of ^{237}Np is near unity.

Again, the present measurements, except perhaps for ^{237}Np, invalidate the use of the photofission reaction alone to determine the total photoabsorption cross section for heavy nuclei. To do this, we would need to measure all of the hadronic decay channels following photoabsorption. Such a detailed investigation of all of the exit channels following photoabsorption would lead to a much better understanding of the microscopic mechanism governing this process.

ACKNOWLEDGMENTS

This work was supported in part by the U.S. Department of Energy under Grant No. DE-FG02-95ER40901 and by the National Science Foundation under Grants No. PHY-9703049 and PHY-9803952. P.L. Cole, W.R. Dodge, V.G. Nedorezov, and A.S. Sudov contributed during various stages of preparing the experimental equipment. We thank those who took shifts during the nine days of data taking: D. Branford, B. Carnahan, K.S. Dhuga, M. Dugger, J.T. O'Brien, B.G. Ritchie, and I.I. Strakovsky. S.A. Philips also helped substantially with the setup in the experimental hall. We were aided in handling the data acquisition system by the expertise of S.P. Barrow. We would like to acknowledge the contribution of the Jefferson Lab staff, especially B.A. Mecking and E.S. Smith, for their advice and support. We thank also G.V. O'Rielly for constructive discussions during the data analysis and for help with the manuscript.

[1] J. T. Caldwell, E. J. Dowdy, B. L. Berman, R. A. Alvarez, and P. Meyer, Phys. Rev. C **21**, 1215 (1980).
[2] H. Ries, G. Mank, J. Drexler, R. Heil, K. Huber, U. Kneissl, R. Ratzek, H. Ströher, T. Weber, and W. Wilke, Phys. Rev. C **29**, 2346 (1984).
[3] B. L. Berman, J. T. Caldwell, E. J. Dowdy, S. S. Dietrich, P. Meyer, and R. A. Alvarez, Phys. Rev. C **34**, 2201 (1986).
[4] J. Ahrens *et al.*, Phys. Lett. **146B**, 303 (1984).
[5] A. Leprêtre *et al.*, Nucl. Phys. **A472**, 553 (1987).
[6] T. Frommhold, F. Streiper, W. Henkel, U. Kneissl, J. Ahrens, R. Beck, J. Peise, and M. Schmitz, Phys. Lett. B **295**, 28 (1992).
[7] B. L. Berman, K. S. Dhuga, and B. G. Ritchie, CLAS Note 92-010, 1992 (unpublished).
[8] N. Bianchi *et al.*, Phys. Rev. C **54**, 1688 (1996).
[9] N. Bianchi, E. De Sanctis, M. Mirazita, and V. Muccifora, Phys. Rev. C **60**, 064617 (1999).
[10] E. A. Arakelyan, A. R. Bagdarsaryan, G. L. Bayatyan, A. R. Voskanyan, N. K. Grigoryan, S. G. Knyazyan, A. T. Margaryan, G. G. Marikyan, and A. K. Papyan, Sov. J. Nucl. Phys. **52**, 878 (1990).
[11] A. S. Iljinov, D. I. Ivanov, M. V. Mebel, V. G. Nedorezov, A. S. Sudov, and G. Y. Kezerashvili, Nucl. Phys. **A539**, 263 (1992).
[12] T. Frommhold *et al.*, Z. Phys. A **350**, 249 (1994).
[13] N. Bianchi *et al.*, Phys. Lett. B **299**, 219 (1993).
[14] J. C. Sanabria, B. L. Berman, C. Cetina, P. L. Cole, G. Feldman, N. R. Kolb, R. E. Pywell, J. M. Vogt, and G. Y. Kezerashvili, Phys. Rev. C **61**, 034604 (2000).
[15] N. Bianchi *et al.*, Phys. Rev. C **48**, 1785 (1993).
[16] J. C. Sanabria, B. L. Berman, C. Cetina, P. L. Cole, G. Feldman, N. R. Kolb, R. E. Pywell, J. M. Vogt, and G. Y. Kezerashvili (unpublished).
[17] J. D. T. Arruda-Neto *et al.*, Phys. Rev. C **41**, 354 (1990).
[18] C. Guaraldo *et al.*, Phys. Rev. C **36**, 1027 (1987).
[19] V. Lucherini *et al.*, Phys. Rev. C **39**, 911 (1989).
[20] M. MacCormick *et al.*, Phys. Rev. C **55**, 1033 (1997).
[21] V. Muccifora *et al.*, Phys. Rev. C **60**, 064616 (1999).
[22] R. C. Carrasco and E. Oset, Nucl. Phys. **A536**, 445 (1992).
[23] T. A. Armstrong *et al.*, Phys. Rev. D **5**, 1640 (1972).
[24] T. A. Armstrong *et al.*, Nucl. Phys. **B41**, 445 (1972).
[25] M. MacCormick *et al.*, Phys. Rev. C **53**, 41 (1996).
[26] M. Anghinolfi *et al.*, Phys. Rev. C **47**, 922 (1993).
[27] W. Weise, Phys. Rep. **13**, 53 (1974).
[28] G. R. Brooks *et al.*, Phys. Rev. D **8**, 2826 (1973).
[29] S. Michalowski, D. Andrews, J. Eickmeyer, T. Gentile, N. Mistry, R. Talman, and K. Ueno, Phys. Rev. Lett. **39**, 737 (1977).
[30] T. Falter, S. Leupold, and U. Mosel, Phys. Rev. C **62**, 031602 (2000).
[31] C. Cetina *et al.*, Phys. Rev. Lett. **84**, 5740 (2000).
[32] D. I. Sober *et al.*, Nucl. Instrum. Methods Phys. Res. A **440**, 263 (2000).
[33] G. Hempel, F. Hopkins, and G. Schatz, Nucl. Instrum. Methods **131**, 445 (1975).
[34] J. D. T. Arruda-Neto, R. Avida, J. R. Calarco, K. A. Griffioen, D. H. H. Hoffmann, K. T. Knöpfle, K. Van Bibber, R. Westerfelt, and J. G. Woodworth, Nucl. Instrum. Methods **190**, 203 (1981).
[35] J. Drexler *et al.*, Nucl. Instrum. Methods **220**, 409 (1984).
[36] P. Garganne, Tech. Rep. Note CEA-N-2492, Centre d'Etudes Nucléaires de Saclay, 1986 (unpublished).

[37] J. C. Sanabria, B. L. Berman, C. Cetina, P. L. Cole, W. R. Dodge, V. G. Nedorezov, A. S. Sudov, and G. Y. Kezerashvili, Nucl. Instrum. Methods Phys. Res. A **441**, 525 (2000).
[38] C. Cetina, Ph.D. thesis, The George Washington University, Washington, DC, 2001.
[39] D. I. Sober (private communication).
[40] J. C. Sanabria, B. L. Berman, P. L. Cole, R. E. Pywell, V. G. Nedorezov, A. S. Sudov, and G. Y. Kezerashvili, Nucl. Instrum. Methods Phys. Res. A **457**, 402 (2001).
[41] P. Heimberg (private communication).
[42] P. Carlos, H. Beil, R. Bergère, J. Fagot, A. Leprêtre, A. De Miniac, and A. Veyssière, Nucl. Phys. **A431**, 573 (1984).
[43] A. S. Iljinov, M. V. Kazarnovsky, and E. Y. Paryev, *Intermediate Energy Nuclear Physics* (CRC Press, Boca Raton, 1994).
[44] I. A. Pshenichnov, A. S. Iljinov, B. L. Berman, W. J. Briscoe, C. Cetina, G. Feldman, and P. Heimberg (unpublished).
[45] N. Bohr and J. Wheeler, Phys. Rev. **56**, 426 (1939).